J. Fluid Mech. (2019), *vol.* 863, *pp.* 341–363.
doi:10.1017/jfm.2018.1000

Direct numerical simulation of backward-facing step flow at $Re_\tau = 395$ and expansion ratio 2

A. Pont-Vílchez[1,†], F. X. Trias[1], A. Gorobets[2] and A. Oliva[1]

[1]Heat and Mass Transfer Technological Centre (CTTC), Universitat Politècnica de Catalunya BARCELONA Tech (UPC) C/ Colom, 11 08222 Terrassa (Barcelona), Spain

[2]Keldysh Institute of Applied Mathematics, 4A, Miusskaya Sq., Moscow 125047, Russia

(Received 23 February 2018; revised 4 October 2018; accepted 5 December 2018; first published online 24 January 2019)

Backward-facing step (BFS) constitutes a canonical configuration to study wall-bounded flows subject to massive expansions produced by abrupt changes in geometry. Recirculation flow regions are common in this type of flow, driving the separated flow to its downstream reattachment. Consequently, strong adverse pressure gradients arise through this process, feeding flow instabilities. Therefore, both phenomena are strongly correlated as the recirculation bubble shape defines how the flow is expanded, and how the pressure rises. In an incompressible flow, this shape depends on the Reynolds value and the expansion ratio. The influence of these two variables on the bubble length is widely studied, presenting an asymptotic behaviour when both parameters are beyond a certain threshold. This is the usual operating point of many practical applications, such as in aeronautical and environmental engineering. Several numerical and experimental studies have been carried out regarding this topic. The existing simulations considering cases beyond the above-mentioned threshold have only been achieved through turbulence modelling, whereas direct numerical simulations (DNS) have been performed only at low Reynolds numbers. Hence, despite the great importance of achieving this threshold, there is a lack of reliable numerical data to assess the accuracy of turbulence models. In this context, a DNS of an incompressible flow over a BFS is presented in this paper, considering a friction Reynolds number (Re_τ) of 395 at the inflow and an expansion ratio 2. Finally, the elongation of the Kelvin–Helmholtz instabilities along the shear layer is also studied.

Key words: shear layer turbulence, turbulence simulation, turbulent convection

1. Introduction

Sudden massive expansions are common in many engineering applications: from internal flows in heat exchangers and combustors to external flows, such as vehicle aerodynamics. Usually, the separation and reattachment processes yield to dramatic drag increases, as well as reductions of the pressure growth and heat transfer rate. Even so, the shear layer can also be beneficial in some industrial applications, triggering turbulence transition and enhancing the mixing rate of chemical species.

† Email address for correspondence: arnau@cttc.upc.edu

In this regard, the backward-facing step (BFS) represents a canonical configuration to study this kind of wall-bounded fluid (see figure 1). This case consists of two channel flows connected by a sharp step of height h. Both channels have the same aspect ratio ($AR = L_z/h$), whereas the difference between the channel heights is defined by the expansion ratio, $ER = H/(H-h)$. Where L_z and H represent the BFS spanwise length and the outlet channel height, respectively. The flow in a BFS is massively separated due to the sudden expansion, but reattached downstream of the channel. The abrupt separation leads to a shear layer which feeds a recirculation bubble attached to the step. This bubble governs the flow progressive expansion downstream of the step edge, as well as the way the pressure grows along the channel (reattachment process). At low Reynolds numbers, the shear layer and the recirculation bubble represents a stable system, as the kinetic energy transferred by the shear layer into the recirculation zone is well dissipated because of the friction forces. However, when the Reynolds is high enough, the viscous forces cannot dissipate all the kinetic energy provided by the shear layer. Thus, the system becomes unstable. Therefore, the inertial forces tend to flap the shear layer, becoming a source of the well-known Kelvin–Helmholtz instabilities (*KH*). Finally, these instabilities are fed, paired and elongated along the shear layer, until they impinge at the lower wall, contributing to the recirculation bubble detachment. Needless to say, the inflow and wall effects also play important roles in all this process.

In addition to its engineering interest, the simplicity of the BFS geometry makes it a suitable case to study the above explained complex phenomena by means of both experimental and numerical analyses. The vast majority of the experimental studies such as Eaton & Johnston (1980), Armaly *et al.* (1983), Driver & Seegmiller (1985), Jovic & Driver (1995) and Kasagi & Matsunaga (1995) were focused on the measurement of the reattachment length (X_r) depending on a single configuration of Reynolds number and *ER*. By contrast, there were only a few researchers such as Kuehn (1980), Durst & Tropea (1981) and Ötügen (1991) who studied the *ER* effects on X_r, using late transitional or turbulent boundary layers at separation. Recently, Nadge & Govardhan (2014) carried out a complete set of parametric studies analysing the influence of the Reynolds number and the *ER* on the X_r. Besides reducing the huge scatter in the data observed in previous studies, the authors also provided results showing the asymptotic behaviour of X_r beyond a certain threshold. It should be noticed here that almost all the experimental works mentioned above followed the De Brederode & Bradshaw (1972) recommendation to avoid the side wall effects ($AR > 10$).

Apart from the large amount of experimental research dedicated during the last decades, numerical simulations are also quite numerous. The first studies, i.e. Speziale & Ngo (1988), Lasher & Taulbee (1992) and Thangam & Speziale (1992), were focused on Reynolds-averaged Navier–Stokes (RANS) models in order to test and improve the existing ones. Once computational resources became more available to the scientific community, less case-dependent methodologies, such as large eddy simulation (LES) and hybrid RANS–LES models, were studied. In particular, the detached eddy simulation (DES) family of models proposed by Spalart *et al.* (1997) in the late 1990s were designed to simulate massively separated flows such as BFS, airfoils at stall and jets. Since then, several authors such as Spalart *et al.* (2006), Shur *et al.* (2008) and Gritskevich *et al.* (2012) focused their efforts on addressing the main two DES shortcomings, which are: the shielding of the RANS boundary layers against any unwanted incursion of the LES formulation and the delay of the *KH* instabilities produced during the RANS to LES transition (Mockett, Haase &

Schwamborn 2018). In this context, the selected BFS configuration ($ER = 2$) presents a challenging configuration where both problematic areas coexist in the same case (DES simulation). In particular, the flow structures (*KH* instabilities) created at the shear layer (LES area) invade the upper wall, damaging the flow behaviour at the boundary layer (RANS area). It is worthwhile pointing out that this phenomenon is negligible if the distance between the LES and RANS area is large enough (low *ER* value).

In spite of the numerous numerical studies using turbulence models, there has been very little research in the BFS area using DNS so far. This fact is mainly due to the computational resources that this sort of simulation requires. First DNS of a fully turbulent BFS was not carried out until the late 1990s, when Le, Moin & Kim (1997) simulated a BFS at $Re_b \sim 4250$ and $ER = 1.2$. Where Re_b is defined using the step height, h, and the inlet bulk velocity, U_b. The authors performed a complete analysis and demonstrated that the log profile downstream of the channel flow was not fully recovered even $19h$ after the reattachment. Their results presented a good agreement with the experiments carried out by Jovic & Driver (1995). Afterwards, other researchers, such as Biswas, Breuer & Durst (2004) and Schäfer, Breuer & Durst (2009), performed DNS to study the BFS flow transition from laminar to turbulent. Both sets of authors used low Reynolds number values and laminar velocity profiles at the inflow. The first author studied a range of small Reynolds numbers, $Re_b \in [5 \times 10^{-5}, 400]$, and expansion ratios, $ER \in [1.9423, 3]$, to detect the transition value at which the turbulence emerges. The second study was focused on the structures created at the step edge of a BFS in a single flow configuration at a higher Reynolds number ($Re_b = 3000$) and $ER = 1.9423$. These authors also studied how those structures were related to the X_r oscillations. However, few authors carried out research at higher Reynolds numbers and using turbulent inflows, such as Meri & Wengle (2002) and Barri *et al.* (2010). The former studied the effect of second- and fourth-order spatial discretization schemes at $Re_b = 3300$ and $ER = 1.5$. The latter used $Re_b = 5600$ and $ER = 2$, studying their inflow approach in a configuration with a non-homogeneous streamwise direction. This turbulent inflow was previously tested in a channel flow by Barri *et al.* (2009), showing a good performance. Although these authors considered different parameters in their simulations, both used the same channel flow configuration at the entrance, $Re_\tau = 180$ (based on the wall skin friction velocity, u_τ, and the half-height of the plane). This is a well-known and widely studied turbulent channel flow, but the low Reynolds number effects are still present. Currently, there is still a lack of numerical data reporting BFS flow behaviour at higher Reynolds numbers, where the low Reynolds number effects are diminished. Moreover, all DNSs carried out so far are significantly far from reaching the X_r asymptotic behaviour.

In this paper, a DNS of an incompressible fluid flow over a BFS with an $ER = 2$ has been performed using a turbulent channel flow at $Re_\tau = 395$ as an inlet condition. Besides being close to reaching an X_r asymptotic behaviour, the studied case is also interesting for understanding how a classical turbulent channel flow is expanded under certain conditions. Regarding the inflow boundary condition, there are two main approaches in order to address this issue. Inflow data can either be generated by previously running a channel flow simulation (as Meri & Wengle 2002 investigated), and saving the velocity field in a streamwise plane or using turbulent synthetic algorithms. The former is used in this paper as it is suitable for performing a DNS. Finally, it is worth noting here that besides giving insights into the physics of turbulent flows after massive separations, the aim of this work consists of providing

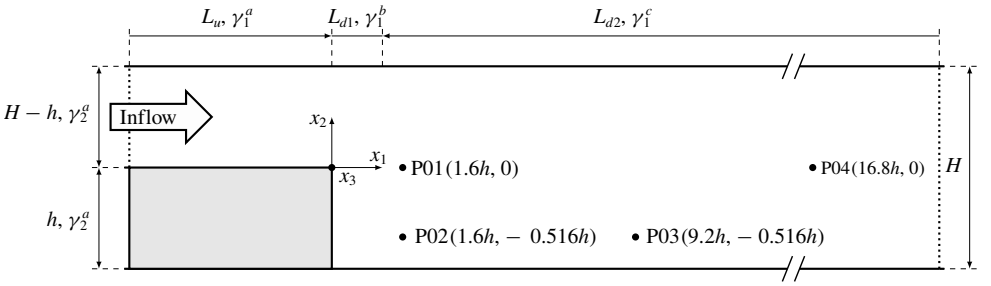

FIGURE 1. Schematic figure of the backward-facing step problem, $ER = H/(H - h) = 2$, and details about its geometry and grid spacing (size of zones and concentration factors; arrows indicate the grid refinement direction). Not to scale.

reference data (Pont-Vílchez *et al.* 2018) for this canonical configuration, and not to reproduce any particular experimental set-up.

The rest of the paper is arranged as follows. In the next section, the governing equations and the problem definition are described together with an overview of the numerical methods. The methodology to verify the simulation is presented in § 3. The core of the results is in § 4. Firstly, the main features of the time-averaged flow are discussed on the basis of a direct comparison with previous experimental results. Reynolds stress transport terms are also presented and commented on in this section. The discussion focuses on the flow dynamics, observing the *KH* instabilities and presenting the kinetic energy spectrum cascade at different flow locations: in the shear layer, recirculation bubble, reattachment and recovery regions. The rate of growth of the *KH* instabilities along the shear layer and their elongation due to the vortex pairing phenomenon are also studied and compared with experimental observations (Winant & Browand 1974; Kostas, Soria & Chong 2002). Finally, the most significant results are summarized and conclusions are given in the last section.

2. Governing equations and numerical methods

The incompressible Navier–Stokes (NS) equations in primitive variables are considered

$$\partial_t u_i + u_j \partial_j u_i = -\partial_i p + \nu \partial_j^2 u_i; \quad \partial_i u_i = 0, \tag{2.1}$$

where u_i is the velocity field, p represents the kinematic pressure and ν is the kinematic viscosity. A schema of the problem under consideration is shown in figure 1.

The dimensions of the computational domain are $38h \times 2h \times 2\pi h$ in the streamwise, normal and spanwise directions, respectively. The sudden expansion is located at $L_u = 6h$ from the inflow, whereas the domain length downstream of the step is divided into two parts ($L_{d1} = 1h$, $L_{d2} = 31h$) for refinement reasons. The origin of coordinates is placed at the expansion sharp edge. A detailed discussion about the determination of the domain size and grid spacing is given in the next section.

Regarding the boundary conditions, a turbulent channel flow is imposed at the inflow following the same strategy used by Meri & Wengle (2002), whereas a convective boundary condition is used at the outflow, $\partial_t u_i + 0.5 U_b \partial_1 u_i = 0$. Global mass conservation may be not exactly preserved after imposing such boundary conditions. It is forced by means of a minor correction (a constant many orders

of magnitude lower than U_b) at the outflow conditions. Finally, periodic boundary conditions are imposed in the spanwise direction, and no-slip boundary conditions are imposed at the walls.

The incompressible NS equations (2.1) are discretized on a non-uniform structured staggered mesh, and a fourth-order symmetry-preserving discretization (Verstappen & Veldman 2003) scheme is used. Briefly, the temporal evolution of the spatially discrete staggered velocity vector, $\boldsymbol{u}_s$, is governed by the following operator-based finite-volume discretization of (2.1),

$$\boldsymbol{\Omega}\frac{\mathrm{d}\boldsymbol{u}_s}{\mathrm{d}t} + \boldsymbol{C}\,(\boldsymbol{u}_s)\,\boldsymbol{u}_s + \boldsymbol{D}\boldsymbol{u}_s - \boldsymbol{M}^t\boldsymbol{p}_c = \boldsymbol{0}_s, \tag{2.2}$$

where the subscripts s, c refer to discrete staggered and collocated vectors, respectively. The discrete incompressibility constraint is given by $\boldsymbol{M}\boldsymbol{u}_s = \boldsymbol{0}_h$, where $\boldsymbol{M}$ indicates the divergence matrix. The diffusive matrix, $\boldsymbol{D}$, is symmetric and positive semi-definite, representing the integral of the diffusive flux, $-\nu\partial_j u_i n_j$, through the faces (where n_j refers to a normal surface direction). The diagonal matrix, $\boldsymbol{\Omega}$, describes the sizes of the control volumes and the approximate, convective flux is discretized as in Verstappen & Veldman (2003). The resulting convective matrix, $\boldsymbol{C}\,(\boldsymbol{u}_s)$, is skew–symmetric, i.e.

$$\boldsymbol{C}\,(\boldsymbol{u}_s) = -\boldsymbol{C}^t\,(\boldsymbol{u}_s). \tag{2.3}$$

In a discrete setting, the skew–symmetry of $\boldsymbol{C}\,(\boldsymbol{u}_s)$ implies that

$$\boldsymbol{C}\,(\boldsymbol{u}_s)\,\boldsymbol{v}_s \cdot \boldsymbol{w}_s = \boldsymbol{v}_s \cdot \boldsymbol{C}^t\,(\boldsymbol{u}_s)\,\boldsymbol{w}_s = -\boldsymbol{v}_s \cdot \boldsymbol{C}\,(\boldsymbol{u}_s)\,\boldsymbol{w}_s, \tag{2.4}$$

for any discrete velocity vector $\boldsymbol{u}_s$ (if $\boldsymbol{M}\boldsymbol{u}_s = \boldsymbol{0}_s$), $\boldsymbol{v}_s$ and $\boldsymbol{w}_s$. The evolution of the discrete energy, $\|\boldsymbol{u}_s\|^2 = \boldsymbol{u}_s \cdot \boldsymbol{\Omega}\boldsymbol{u}_s$, is governed by

$$\frac{\mathrm{d}}{\mathrm{d}t}\|\boldsymbol{u}_s\|^2 = -2\boldsymbol{u}_s \cdot \boldsymbol{D}\boldsymbol{u}_s < 0, \tag{2.5}$$

where the convective and pressure gradient contributions cancel because of (2.3) and the incompressibility constraint, $\boldsymbol{M}\boldsymbol{u}_s = \boldsymbol{0}_c$, respectively. Therefore, even for coarse grids, the energy of the resolved scales of motion is convected in a stable manner, i.e. the discrete convective operator transports energy from a resolved scale of motion to other resolved scales without dissipating any energy, as it should be from a physical point of view. For a detailed explanation, the reader is referred to Verstappen & Veldman (2003).

The governing equations are integrated in time using a classical fractional step projection method (Chorin 1968). Namely, the solution of the unsteady Navier–Stokes equations is obtained by first time advancing the velocity field, $\boldsymbol{u}_s^n$, without regard for its solenoidality constraint, then recovering the proper solenoidal velocity field, $\boldsymbol{u}_s^{n+1}$ ($\boldsymbol{M}\boldsymbol{u}_s = \boldsymbol{0}_c$). For the temporal discretization, a second-order fully explicit one-leg scheme is used for both the convective and diffusive terms (Trias & Lehmkuhl 2011). Thus, the resulting fully discretized problem reads

$$\frac{(\kappa + 1/2)\boldsymbol{u}_s^p - 2\kappa\boldsymbol{u}_s^n + (\kappa - 1/2)\boldsymbol{u}_s^{n-1}}{\Delta t} = \boldsymbol{R}((1+\kappa)\boldsymbol{u}_s^n - \kappa\boldsymbol{u}_s^{n-1}), \tag{2.6}$$

where $\boldsymbol{R}(\boldsymbol{u}_s) = -\boldsymbol{C}\,(\boldsymbol{u}_s)\,\boldsymbol{u}_s - \boldsymbol{D}\boldsymbol{u}_s$ and $\boldsymbol{u}_s^p$ is a predictor velocity that can be directly evaluated from the previous expression. The time-integration parameter, κ, is

computed to adapt the linear stability domain of the time-integration scheme to the instantaneous flow conditions in order to use the maximum time step possible. For further details about the time-integration method the reader is referred to Trias & Lehmkuhl (2011). Finally, $\boldsymbol{u}_s^p$ must be projected onto a divergence-free space,

$$\boldsymbol{u}_s^{n+1} = \boldsymbol{u}_s^p + \boldsymbol{\Omega}^{-1}\boldsymbol{M}^t\tilde{\boldsymbol{p}}_c^{n+1}, \tag{2.7}$$

by adding the gradient of the pseudo-pressure, $\tilde{\boldsymbol{p}}_c = \Delta t/(\kappa + 1/2)\boldsymbol{p}_c$, satisfying the following Poisson equation

$$\boldsymbol{L}\tilde{\boldsymbol{p}}_c^{n+1} = \boldsymbol{M}\boldsymbol{u}_s^p \quad \text{with } \boldsymbol{L} = -\boldsymbol{M}\boldsymbol{\Omega}^{-1}\boldsymbol{M}^t, \tag{2.8}$$

where the discrete Laplacian operator, $\boldsymbol{L}$, is represented by a symmetric negative semi-definite matrix. For details about the numerical algorithms and the parallel Poisson solver, the reader is referred to Gorobets, Trias & Oliva (2013). Notice that the pressure is not considered in the prediction step (2.6). On staggered grids with prescribed velocity boundary conditions, as in this case, the incompressibility condition occurs naturally and no specific boundary condition for the discrete pressure field, $\boldsymbol{p}_c$, needs to be specified, as pointed out in Kim & Moin (1985). Nevertheless, Neumann boundary conditions are prescribed for $\boldsymbol{p}_c$. Regarding the verification of the code, the reader is referred, for example, to Trias *et al.* (2007). The verification process of the DNS simulation carried out in this work is addressed in the next section.

3. Verification of the simulation

Averages over the two statistically invariant transformations (time and x_3-direction) are carried out for all the fields. The standard notation $\langle\cdot\rangle$ is used to denote this averaging procedure.

During this section, the DNS results are verified using well-known tests in the literature. They are mainly focused on BFS, but the inflow quality is firstly discussed. As was mentioned before, the inflow data are obtained from a previous channel flow simulation at $Re_\tau = 395$. The signal is preprocessed before being used by the BFS. A linear spatial interpolation is applied as a slightly coarser mesh is used in the BFS case because of computational cost reasons. The quality of the preprocessed inflow is assessed in figure 2, where the average streamwise velocity (a) and the root mean square (r.m.s.) (b) profiles at a certain cross-section ($-5h$) over the step are presented. They show a good agreement with the benchmark case (Moser, Kim & Mansour 1999). A short distance from the inflow is selected ($6h - 5h = h$) to demonstrate that there is no need for a recovery region when this method is applied.

Once the behaviour of turbulence at the entrance is assessed, the minimum time integration period is determined. This has been achieved evaluating the normalized infinite norm of the first-, second- and third-order tensor turbulent statistic values at each time step (3.1).

$$\|A\|_{o,\infty}(t_s) = \max_n^N \left| 1 - \frac{1}{\langle a_{o,n}\rangle} \int_0^{t_s} a_{o,n}\,\mathrm{d}t \right|, \tag{3.1}$$

where $[a_o]$ denotes a list of N elements, which depends on the order (o), and n refers to a specific list element, $a_{o,n}$. The symbology $[\cdot]$ converts any tensor in a list of elements. Elements presenting average values, $\langle a_{o,n}\rangle$, close to zero are excluded

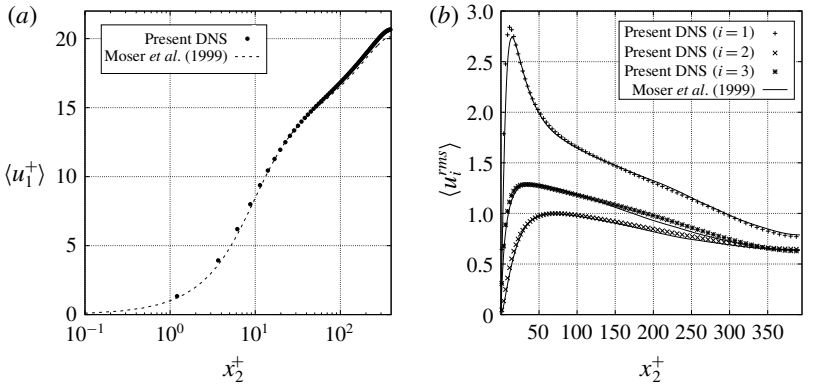

FIGURE 2. Average streamwise velocity (*a*) and root-mean-square (*b*) profiles at $-5h$ over the step ($1h$ downstream of the inflow). Moser *et al.* (1999) results are used as benchmark data.

in order to avoid 0/0 indeterminate forms. The maximum absolute value in a list of N elements is selected at each t_s, and denoted as $\|A\|_{o,\infty}(t_s)$. For instance, the first-order list ($N = 3$) is filled by all velocity components ($[a_1] = [u_i]$), whereas the second-order list ($N = 9$) includes all second-order tensor elements ($[a_2] = [u_i u_j]$). The same explanation is valid for the third-order list. A set of probes has been distributed along the domain, but only the most important ones are shown in figures 1 and 3. The largest integration period is required at P04, where large structures dragged from the recirculation region are present. Similar behaviour is observed in the shear layer region, P01, where high velocity fluctuations also appear. The rest of the probes are located between the two recirculation bubbles, P02, and in the reattachment region, P03. A schematic view of the probes location can be observed in figure 1. In contrast to the 280 average integration time units (h/u_τ) suggested by Barri *et al.* (2010), figure 3 shows that $180h/u_\tau$ provides satisfactory results. This simulation time reduction can be attributed to the fact that different time integration techniques are applied. A set of individual quasi-independent flow fields separated by $0.25h/u_\tau$ were taken into account by Barri *et al.* (2010), whereas a continuous integration with time is used in the present paper. Apart from that, other factors, such as the Re_τ, could also affect the integration time period. From here on, all time-average results presented in this paper have been obtained using $180h/u_\tau$, around 55 flow units ($t_f = (L_u + L_d ER)/U_b$).

The BFS geometry in the spanwise and streamwise directions is also studied because of its influence in the fluid behaviour. The capability of the spanwise length to reproduce the larger scales is assessed through two-point correlations, $B_i^{norm}(x_3 = 0, \hat{x}_3) = B_i^{norm}(\hat{x}_3)$, at the locations shown in figure 1:

$$B_i^{norm}(x_j, \hat{x}_j) = \frac{\langle u_i'(x_j) u_i'(x_j + \hat{x}_j) \rangle}{\langle u_i'(x_j) \rangle \langle u_i'(x_j + \hat{x}_j) \rangle}. \tag{3.2}$$

All velocity components present correlations no longer than the periodic half-length (see figure 4). Thus, the periodic direction requirement is satisfied. The largest structures appear in the recirculation bubble (P02), where the fluid becomes quasi-laminar, and the recovery region (P04). Furthermore, the streamwise length is also examined as some experimental works, such as Nadge & Govardhan (2014),

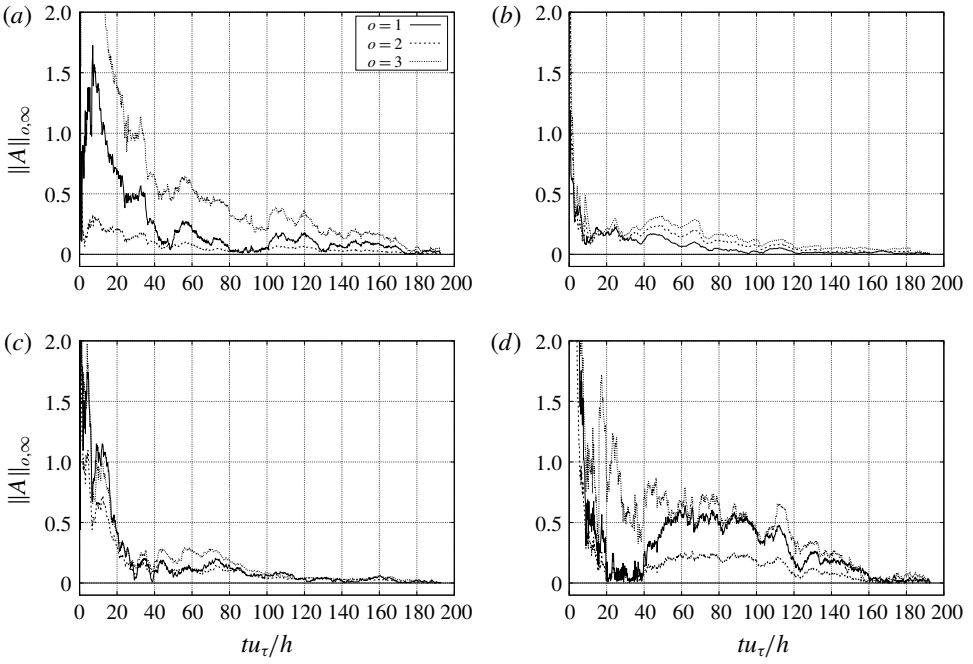

FIGURE 3. Normalized infinite norm ($\|A\|_{o,\infty}$) (defined in (3.1)) of the first, second and third order of the non-zero velocity turbulent statistic at P01 (*a*), P02 (*b*), P03 (*c*) and P04 (*d*). Probe locations are defined in figure 1.

reported a systematic increase of the X_r and the recovery region under the step when the Re was increased. In particular, Nadge demonstrated that this trend exists up to $Re_b \approx 16300$. Beyond this threshold, the X_r only depends on the ER. In the present paper, and despite the recirculation length increase with respect to the case studied by Barri *et al.* (2010), the recirculation zone remains far enough to be affected by the outflow effects. More information regarding the streamwise length can be obtained in § 4.

Once the physical parameters are controlled, the grid resolution and the time step need to be determined. A Cartesian staggered mesh with $1510 \times 302 \times 360$ grid points has been used to cover the computational domain. The grid spacing in the periodic x_3-direction is uniform, whereas the rest of the directions use piecewise hyperbolic–tangent functions. For example, the distribution of points in the x_2-direction corresponding to the step region, i.e. $-h \leqslant x_2 \leqslant 0$, is given by

$$x_{2,k} = x^a_{2,0} + \frac{h}{2}\left(1 + \frac{\tanh\{\gamma^a_2(2(k-1)/N_2 - 1)\}}{\tanh\gamma^a_2}\right), \quad k = 1, \ldots, N_2 + 1, \tag{3.3}$$

where the starting point, the number of grid points and the refinement factor are $x^a_{2,0} = -h$, $N_2 = 302/2$ and $\gamma^a_2 = 1.16855$. The same is true above the step region, but using $x^a_{2,0} = 0$. In these regions, the mesh is refined in both directions. The grid refinement formula needs to be properly adapted for those areas where the mesh is refined only in one direction (see figure 1 for details). For example, the grid points in the region upstream of the step, i.e. $-L_u \leqslant x_1 \leqslant 0$, are distributed as follows

$$x_{1,k} = x^l_{1,0} + \frac{L^l_1}{2}\left(1 + \frac{\tanh\{\gamma^l_1((k-1)/N^l_1 - 1)\}}{\tanh\gamma^l_1}\right), \quad k = 1, \ldots, N^l_1 + 1, \tag{3.4}$$

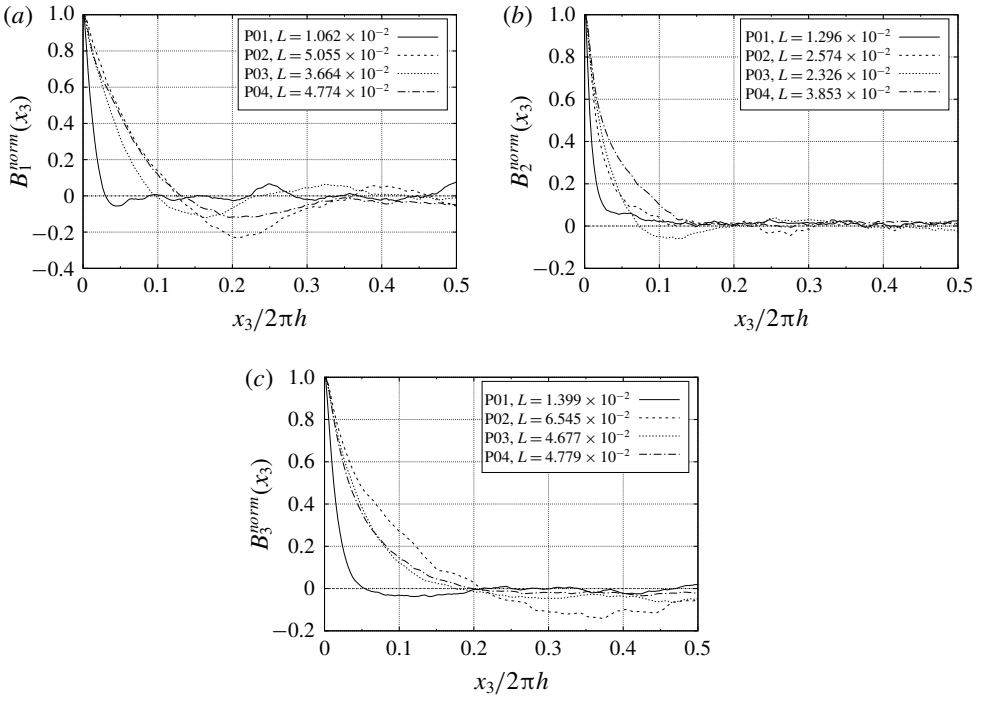

FIGURE 4. Two-point correlation in the spanwise direction of three velocity components at P01, P02, P03 and P04 locations (see figure 1). The integral scale value (L) of each cross-correlation is presented at the legend. Streamwise (a), normal (b) and spanwise (c) components.

where l refers to the zone which is being studied (a, b, c). In this case $l = a$, while the starting point, the region length and the refinement factor are $x^a_{1,0} = -L_u$, $L^a_1 = L_u$ and $\gamma^a_1 = 1.1$, respectively. The same technique is applied in the outflow region ($l = c$), where $x^c_{1,0} = L_{d1}$ and $\gamma^c_1 = 1.5$. There are no arrows in region $l = b$, as a uniform distribution is imposed in order to increase the mesh resolution in this area and to capture the shear layer phenomena. Finally, the number of grid points follows straightforwardly by imposing that $N^a_1 + N^b_1 + N^c_1 = N_1 = 1510$, and that the sizes of two consecutive control volumes corresponding to different areas are equal. The grid points in the x_2-direction are distributed following the same restrictions.

Mesh quality has been assessed using the present DNS results, analysing the control volume size next to the wall and at the core. The former is evaluated using wall units, whereas a comparison with the estimated Kolmogorov length scales is performed with the latter. Figure 5 presents the mesh dimensions in wall units at the upper and lower walls along the streamwise direction. It can be noticed that the mesh refinement at the lower wall upstream of the step ($x_1 \leqslant 0$) has not been provided as it exhibits a similar behaviour to the upper wall (difference less than 1.5 %). Hence, figure 5 shows how the selected mesh is fine enough in all directions to perform a channel flow DNS upstream and downstream of the step edge. In particular, the mesh dimension in the normal direction is $\Delta x_2^+ \lesssim 1.3$. A mesh decrease in wall units is observed in all directions just under the step (lower wall) due to the fact that the recirculation bubbles smooth the velocity gradients close to the wall. Although this decrease also

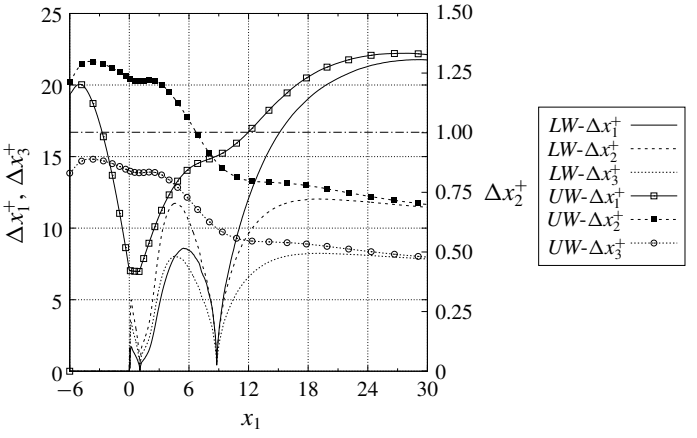

FIGURE 5. Mesh dimensions next to the upper (*UW*) and lower (*LW*) walls expressed in wall units ($\delta_+ = \nu/u_\tau$).

affects Δx_1^+, its reduction is mainly caused by the mesh refinement in order to capture the well-known massive expansion phenomenon. It is worth noting here that both walls lead to the same channel flow behaviour far away from the step edge (recovery region).

Regarding the mesh quality at the core of the BFS, the ratio of different spatial length scales versus the estimated Kolmogorov length scale, $\eta = (\nu^3/\langle\varepsilon\rangle)^{1/4}$, have been evaluated in the sudden expansion zone. Where $\langle\varepsilon\rangle$ refers to the turbulent kinetic energy dissipation term. The spatial length scale would define the smallest scales that can be created in a given mesh, which not only depends on the mesh itself but also on the flow behaviour. In this context, two common approaches for assessing the spatial length scales are considered: the ratio of the maximum local control volume dimension, $\Delta_{max} = \max(\Delta x_1, \Delta x_2, \Delta x_3)$, and the cube root of the cell volume, $\Delta_\forall = (\Delta x_1 \Delta x_2 \Delta x_3)^{1/3}$. The former is preferable in zones with isotropic-like turbulence, while the latter performs better in zones where important anisotropies are present (Shur *et al.* 2015). The effects of the spatial length scale in the sudden expansion zone can be observed in figure 6, where the ratio values using both scales are displayed. First, the highest values in both (*a*) and (*b*) are located downstream of the step edge and at the reattachment zone. The former is caused by the shear layer effects, while the latter is attributed to the mesh coarsening in the streamwise direction. In addition, the ratio Δ_{max}/η (*a*) generally presents higher values than $\Delta_\forall/\eta$ (*b*).

It is worth noting here that, even though Δ_{max}/η (*a*) is considerably larger at the shear layer, it is not a suitable criterion due to the high flow anisotropies (two-dimensional-like). Therefore, in this case the $\Delta_\forall$ (*b*) ratio would be more representative. The contrary is true downstream of the shear layer, at the core of the channel, where the flow starts the recovery process. In any case, values higher than 10 are not observed, which is similar to the resolution requirements discussed by Trias, Gorobets & Oliva (2015). In this regard, a recent work carried out by Vreman & Kuerten (2014) has shown that most of the dissipation in a turbulent channel flow occurs at scales greater than 30η. Finally, a good agreement with the results provided by Meri & Wengle (2002) has also been observed, although these authors provided only shorthand information regarding this verification part.

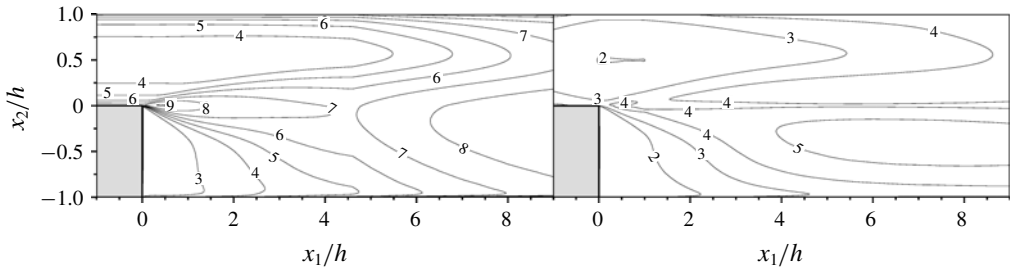

FIGURE 6. Mesh quality assessment, comparing different local spatial scales with the Kolmogorov length scale, η. Those are: the maximum local control volume dimension (*a*), Δ_{max}, and the cell volume cube root (*b*), $\Delta_\forall$.

4. Results and discussion

The average flow fields and the time-dependent signals collected during the simulation are discussed in this section. For the sake of clarity, this work only contains the most significant results according to the authors' criterion. All data obtained in this research are publicly available on the internet (Pont-Vílchez *et al.* 2018).

4.1. *Time-averaged flow*

The pressure coefficient distribution, $\langle C_p \rangle = (\langle p \rangle - p_o)/(1/2)U_c^2$, the velocity components and the streamlines of the average flow in the recirculation region are shown in figure 7. Here, p_o refers to the kinematic pressure at the step edge. The sudden expansion leads to a massive flow separation (*c*), and its respective adverse pressure gradient (*a*). The velocity field distribution (*b*) is consistent with the pressure rise and the streamlines. Velocity components are depicted in a different manner in order to improve visualization and provide a dynamic perception. The $\langle C_p \rangle$ rise at the lower wall across the streamwise direction is detailed in figure 8(*b*). DNS data show a good agreement in comparison to the experimental work carried out by Ötügen (1991), although higher adverse pressure gradients were detected by this author. The skin friction, $\langle C_f \rangle = \langle \tau_w \rangle/(1/2)\rho U_c^2$, is also presented in the same figure at the upper and lower walls (*a*), and compared to the numerical DNS results obtained by Barri *et al.* (2010) ($Re_\tau = 180$, $ER = 2$). Regarding the Jovic & Driver (1995) study, a significant reduction of the $\langle C_f \rangle$ negative peak located at the lower wall (*LW*) is perceived when the Re_b increases. This points out a depletion of the diffused momentum in the recirculation region with respect to the amount of momentum that is entering through the inflow. According to the literature, the X_r elongation phenomenon is also observed, exhibiting an X_r equal to $8.8h$ at $Re_\tau = 395$ and $7.1h$ at $Re_\tau = 180$. This trend is detailed in figure 9, where the DNS results of different authors are compared with the experimental results obtained by Nadge & Govardhan (2014). The present DNS is not only close to the asymptotic region, but also exhibits a good agreement with the experimental data (relative difference $\leqslant 3.5\,\%$). It is worth noting that the X_r value reported by Ötügen (1991) is not presented in this figure as the author evaluated this coefficient considering other methodologies. Even so, not all results provided by Ötügen (1991) have been disregarded, such as the streamwise velocity and r.m.s. profiles, which have been compared with the present DNS at different locations in figure 10. Although some differences can be observed, an acceptable agreement is

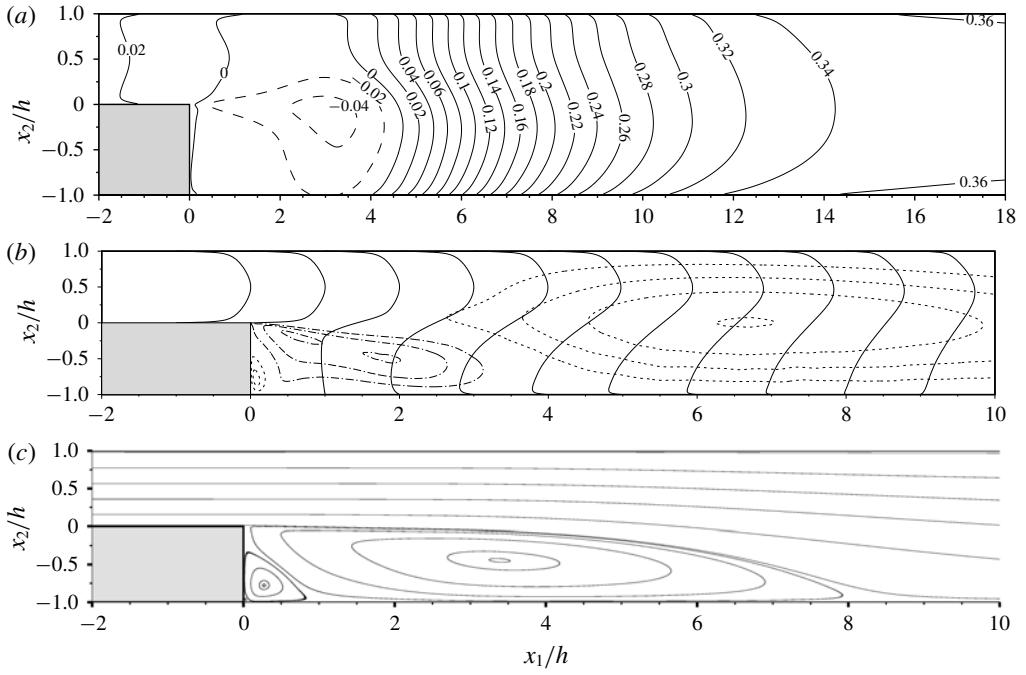

FIGURE 7. (*a*) Pressure coefficient distribution, $\langle C_p \rangle$, (*b*) the average velocity field, $\langle u_i \rangle$, and (*c*) flow streamlines in the recirculation region. For the sake of clarity, the streamwise velocity, $\langle u_1 \rangle$, is indicated using solid lines, whereas the normal velocity component, $\langle u_2 \rangle$, is depicted using isolines (where dashed lines denote positive values and dot-dashed lines denote negative ones). The $\langle u_1 \rangle$ values have been normalized using the maximum velocity of each profile, following the Ötügen (1991) criterion.

present in both variables. The discrepancies observed between the experimental and numerical data could be related to the important scattering registered by Nadge & Govardhan (2014). The author reflected his concerns about this topic, concluding that other elements in addition to the Reynolds number and the *ER* could affect the massive expansion behaviour. In particular, the flow performance just before the sudden expansion is considered an influential factor, although it has not been commonly reported in the literature. In this paper a $Re_\tau = 400.5$ and a turbulence intensity in the streamwise direction equal to $u_{rms}/U_c \approx 3.8\,\%$ are observed. Hence, the lack of agreement observed in figure 10 could be attributed to the fluid behaviour misalignments at the step edge.

The strong turbulence behaviour presented in this BFS configuration is quantified through the Reynolds stresses, as well as the production and dissipation terms derived from their respective transport equations.

$$\underbrace{\partial_t \langle u_i' u_j' \rangle}_{\simeq 0} + \underbrace{\langle u_k \rangle \partial_k \langle u_i' u_j' \rangle}_{Convection} = \underbrace{\langle P_{ij} \rangle}_{Production} + \underbrace{\langle \Pi_{ij} \rangle}_{Pressure-Strain} + \underbrace{\langle D_{ij} \rangle}_{Diffusion\ \ Terms} - \underbrace{\langle \varepsilon_{ij} \rangle}_{Dissipation}, \tag{4.1}$$

where:

$$\langle P_{ij} \rangle = -\langle u_i' u_k' \rangle \partial_k \langle u_j \rangle - \langle u_j' u_k' \rangle \partial_k \langle u_i \rangle, \tag{4.2a}$$

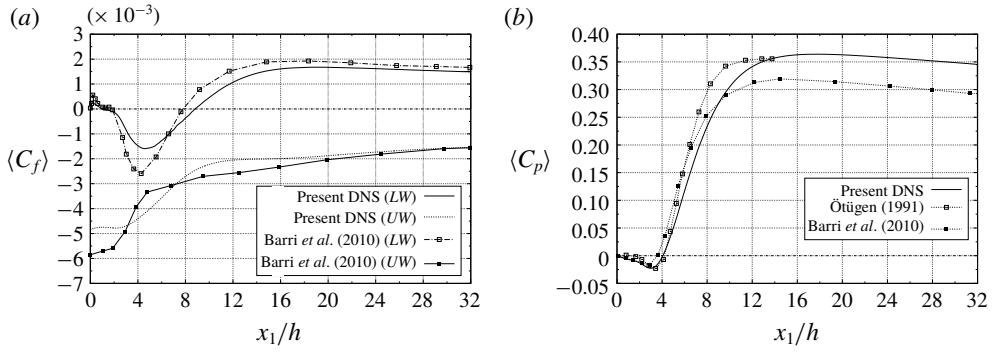

FIGURE 8. Comparison of the skin friction (*a*), $\langle C_f \rangle$, at $Re_\tau = 395$ (present DNS) with the results obtained by Barri *et al.* (2010) at $Re_\tau = 180$ using an $ER = 2$. The $\langle C_f \rangle$ is assessed at the lower (*LW*) and upper (*UW*) walls. Pressure coefficient (*b*), $\langle C_p \rangle$, at the *LW* obtained in the present DNS compared to the results provided by Barri *et al.* (2010), $Re_\tau = 180$, and Ötügen (1991), $Re_\tau = 395$.

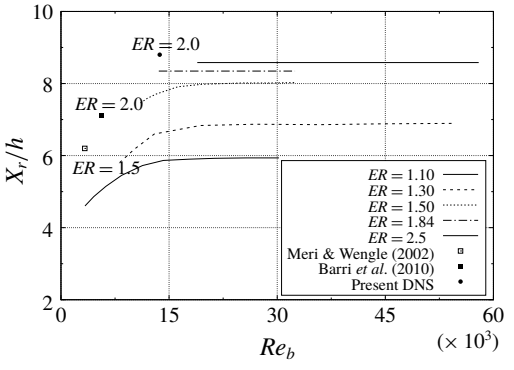

FIGURE 9. Recirculation length (X_r) using different Reynolds numbers (Re_b) and expansion ratios (*ER*). Experimental results depicted by lines were obtained by Nadge & Govardhan (2014).

$$\langle \Pi_{ij} \rangle = \langle p'(\partial_j u_i' + \partial_i u_j') \rangle, \tag{4.2b}$$

$$\langle D_{ij} \rangle = -\partial_k [\langle u_i' u_j' u_k' \rangle + (\langle p' u_j' \rangle \delta_{ik} + \langle p' u_i' \rangle \delta_{jk}) - \nu \partial_k \langle u_i' u_j' \rangle], \tag{4.2c}$$

$$\langle \varepsilon_{ij} \rangle = 2\nu \langle \partial_k u_i' \partial_k u_j' \rangle. \tag{4.2d}$$

In order to simplify the analysis process, only the non-zero components are depicted and nearly the same layout as used by Barri *et al.* (2010) is considered. A general increase of the Reynolds stresses is well observed in all directions in comparison to the Barri *et al.* (2010) results. A downstream shifting of the Reynolds stress zero-gradient area can also be appreciated.

The highest momentum oscillations are in the streamwise direction, $\langle u_1' u_1' \rangle$, as can be noticed in figure 11(*a*). This turbulence, which is triggered by the huge source term (*b*), is balanced by the isotropization behaviour of the pressure–strain (*c*). In fact, the energy from the most energetic component (streamwise) is distributed to the weakest ones (normal and spanwise directions) because of the pressure–strain phenomenon. In

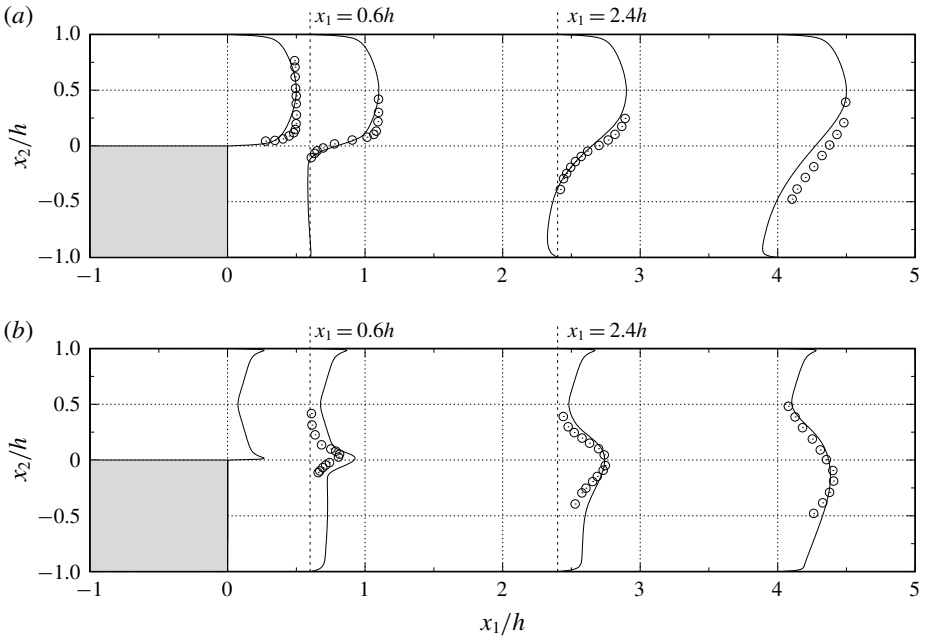

FIGURE 10. Streamwise velocity (a) and r.m.s. (b) profiles of the present DNS (——) compared to the experimental results ($\odot$) obtained by Ötügen (1991). Velocity (u_1) and r.m.s. values are normalized using the maximum value at each profile, U_c.

contrast to the channel flow behaviour, some positive values appear in the impinging regions. They are located at the end of the recirculation length and at the lower part of the shear layer. In both cases, the velocity in the streamwise direction is accelerated $\partial_1 u_1$, whereas a pressure positive peak arises from the impinging interactions. As was expected, the dissipation term, $\langle \varepsilon_{11} \rangle$, is positive and achieves its maximum values in the shear layer and close to the walls. At the lower wall, the opposite is true due to the oscillations and gradient reduction at the recirculation bubble zone.

Fluctuations in the normal direction, $\langle u_2' u_2' \rangle$, are shown in figure 12(a). Although in this case they are less energetic in comparison to $\langle u_1' u_1' \rangle$, they remain significant. The production term (b) is non-zero, in contrast to a channel flow, and significantly lower than the pressure–strain (c). The dissipation term (d) is also positive and, as was expected, stronger in the shear layer and close to the walls.

The periodic nature of the spanwise direction, $\langle u_3' u_3' \rangle$, leads to an absence of the production term. However, the oscillations in this direction (see figure 13a) are nearly as vivid as the streamwise ones. This phenomenon occurs because of the isotropization effect of the pressure–strain tensor, which converts the $\langle u_1' u_1' \rangle$ fluctuations into $\langle u_3' u_3' \rangle$ ones. The dissipation (c) term presents the same trend the above-mentioned Reynolds stresses.

In order to complete the Reynolds stress assessment, the Reynolds stress non-zero cross-term ($-\langle u_1' u_2' \rangle$) is depicted in figure 14(a). The classic axisymmetry presented in a channel flow is lost downstream of the step, but slowly recovered after the reattachment. Although this term does exhibit rather weak values (a) in comparison to the other stresses, the production (b) and pressure–strain (c) terms are quite energetic. Both terms almost present a complementary behaviour in the shear layer, explaining why the dissipation term in this zone is nearly zero.

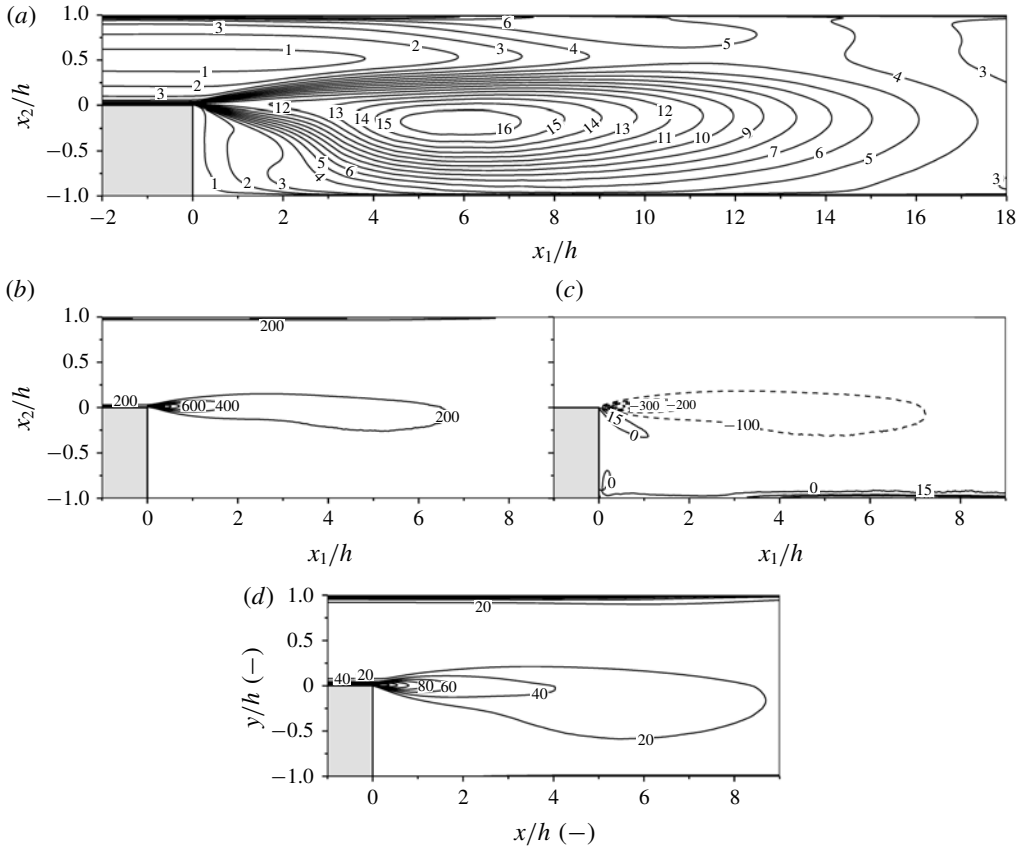

FIGURE 11. Reynolds stresses $\langle u_1' u_1' \rangle / u_\tau^2$ (*a*) and their associated transport source–sink terms scaled using u_τ^3/h: production $\langle P_{11} \rangle$ (*b*), pressure–strain $\langle \Pi_{11} \rangle$ (*c*) and dissipation $\langle \varepsilon_{11} \rangle$ (*d*). Dashed lines depict negative values.

4.2. *Flow dynamics*

Once the average time properties have been analysed, the time-dependent variables are assessed. An idea of the flow dynamics is given in figure 15, where the pressure gradient magnitude in the recirculation zone is shown. First, *KH* structures are visualized just after the sharp edge (*b*), leading to the highest Reynolds stress values in the BFS domain (see figures 11–14). In contrast, a particular lack of pressure gradient is observed in the secondary recirculation bubble region due to its non-turbulent behaviour. Additional information is provided in the film (Pont-Vílchez *et al.* 2018), i.e. the slow motion of the recirculation bubble flow and the progressive expansion of the mainstream flow downstream of the step. The sudden expansion effects on the flow topology can also be noticed in the normal view at $x_2^+ = 1$ in figure 16. For instance, the turbulence triggering produced by the step edge are visualized with the Q-invariant (*a*), showing how the highest intensity is located just downstream of the expansion. Furthermore, the channel flow streaks are also well observed in figure 16(*b*,*c*) until the sudden expansion. Downstream of the step edge, nearly 'two-dimensional' coherent structures are shown from 0 up to $\sim 0.5h$ in u_2' (*b*). Beyond this threshold, the 'two-dimensional' coherence is lost, but the structures still grow. A similar behaviour can be observed in u_1' (*c*).

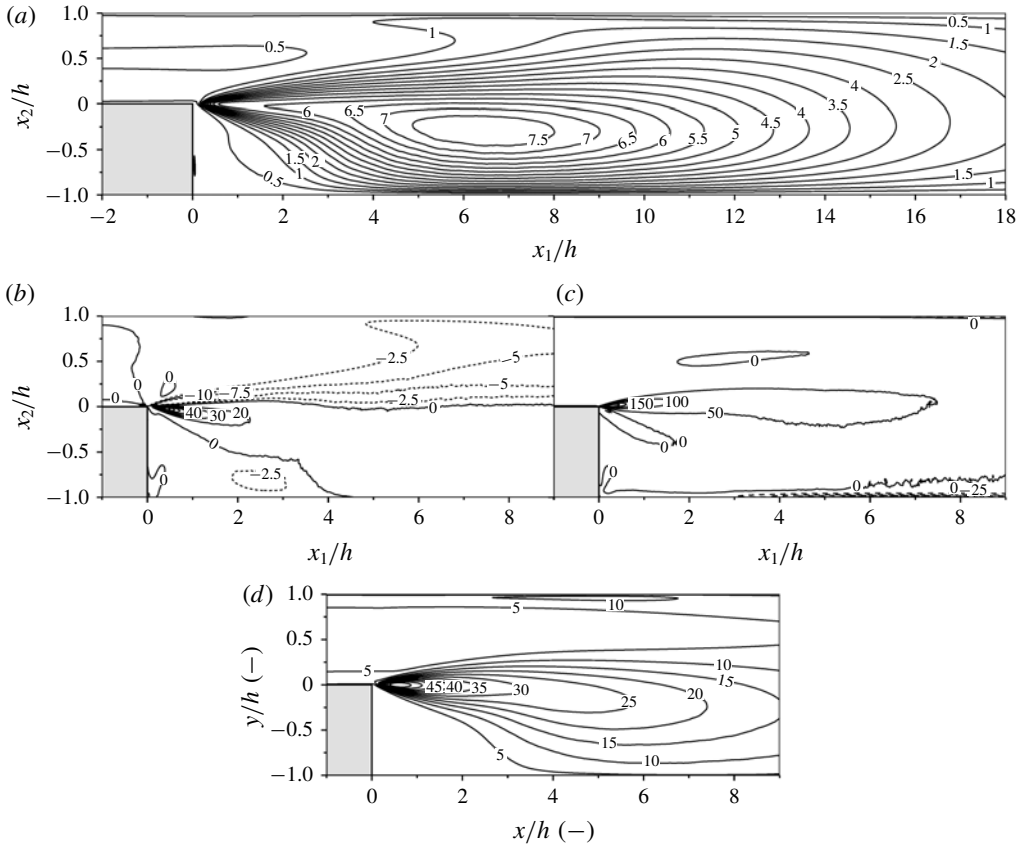

FIGURE 12. Reynolds stresses $\langle u_2' u_2' \rangle / u_\tau^2$ (*a*) and their associated transport source–sink terms scaled using u_τ^3/h: production $\langle P_{22} \rangle$ (*b*), pressure–strain $\langle \Pi_{22} \rangle$ (*c*) and dissipation $\langle \varepsilon_{22} \rangle$ (*d*). Dashed lines depict negative values.

Besides the turbulence triggered at the step edge and its respective spreading, figures 15 and 16 also display a significant flow heterogeneity. In order to assess such diversity of flow regimes, the turbulent kinetic energy cascade at different locations has been considered (see figure 17). A schematic view of the probe locations can be observed in figure 1. Unfortunately, *KH* instabilities are not well captured in figure 17(*a*), as their low energy structure effects can be easily hidden by turbulent scales coming from the channel flow boundary layer. Even so, a good trend is observed in the inertial zone ($\bar{f}^{-5/3}$). It is worth noting here that the P02 frequency cascade has not been included in this figure, as the probe is located in a quasi-laminar region. Regarding the rest of $\bar{f}^{kmg}$ shown in figure 17, they diminish in the downstream direction because of the sudden expansion (P03, P04). Due to the fact that the spatial scale is *ER* times higher at the outflow, the flow moves *ER* times slower in order to ensure the mass conservation. Consequently, the time scale is decreased by a factor of ER^2, bringing out the $\bar{f}^{kmg}$ trend observed (these relations can be easily demonstrated through dimensional analysis).

Even though the ejection frequency of the *KH* instabilities has not been well captured in P01, other interesting shear layer properties have been discerned, such as the *KH* rates of growth along the streamwise direction. A schematic view of a shear

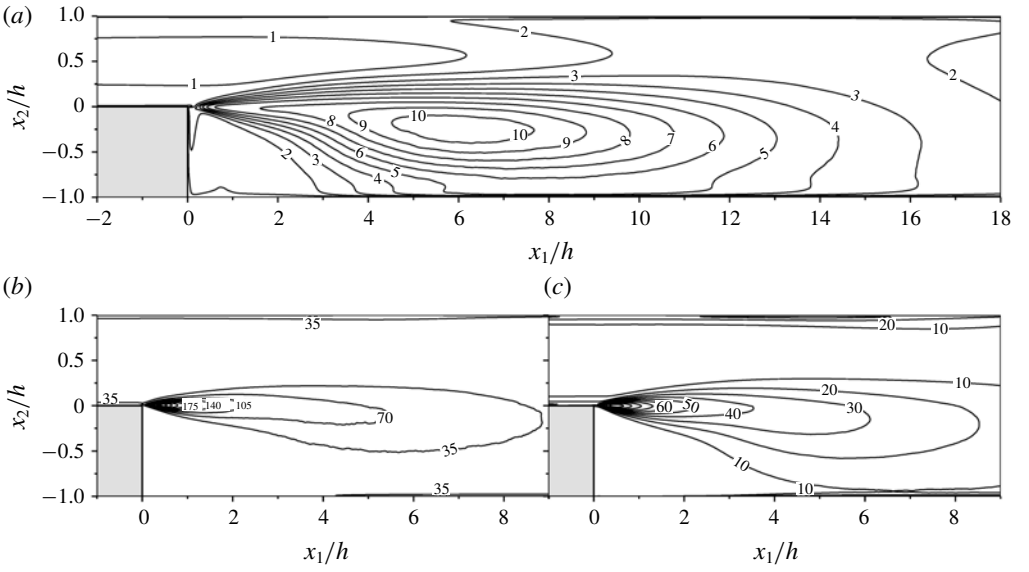

FIGURE 13. Reynolds stresses $\langle u_3' u_3' \rangle / u_\tau^2$ (a) and their associated transport source–sink terms scaled using u_τ^3/h: pressure–strain $\langle \Pi_{33} \rangle$ (b) and dissipation $\langle \varepsilon_{33} \rangle$ (c). Dashed lines depict negative values.

layer is presented in figure 18, showing different structures' size in the streamwise ($\Delta\delta_1$) and normal ($\Delta\delta_2$) directions.

This vortex elongation was mainly attributed to the advection velocity and the vortex pairing phenomenon, which was studied by Winant & Browand (1974). In particular, an elliptic-like shape was experimentally detected, observing a major-to-minor axis ratio of $\Delta\delta_1/\Delta\delta_2 \sim 2$. This behaviour has been analysed with the present DNS data through the two-point correlation technique in the streamwise and normal directions. In the $\Delta\delta_1$ case, the distance from peak to peak (upstream) has been used to represent the distance between vortices (figure 19a) and also to form an estimation of the average vortex size in a given position, $B_2^{norm}(x_1, \hat{x}_1)$. In contrast, $\Delta\delta_2$ has been measured as the distance between zero values of the two-point correlation values, $B_1^{norm}(x_2 = 0, \hat{x}_2)$. In addition, $\Delta\delta_2$ has also been assessed following the equation given in Winant & Browand (1974),

$$\Delta\delta_2 = \Delta U_1 / (\partial \langle u_1 \rangle / \partial x_2)_{max}, \tag{4.3}$$

where ΔU_1 refers to the flow velocity difference in the shear layer.

Two linear distributions for $\Delta\delta_1$ and $\Delta\delta_2$ have been obtained through the two-point correlation technique, showing circular structures ($\Delta\delta_1 \sim \Delta\delta_2$) just downstream of the step edge ($\sim 0.4h$). This is in good agreement with the 'two-dimensional' coherent structures observed in figure 16. Above this threshold, the circular structures are distorted, acquiring an elliptic shape ($\Delta\delta_1 > \Delta\delta_2$), which can be attributed to the above mentioned phenomena. This elliptical shape trend seems to be maintained along the studied domain, showing a major-to-minor axis ratio limit close to 2 ($\Delta\delta_1/\Delta\delta_2$), strengthening the experimental visualizations carried out by Winant & Browand (1974) and supporting their theory regarding the vortex pairing (Pont-Vílchez *et al.* 2018). It is worth noting that Kostas *et al.* (2002) observed a similar phenomenon in their

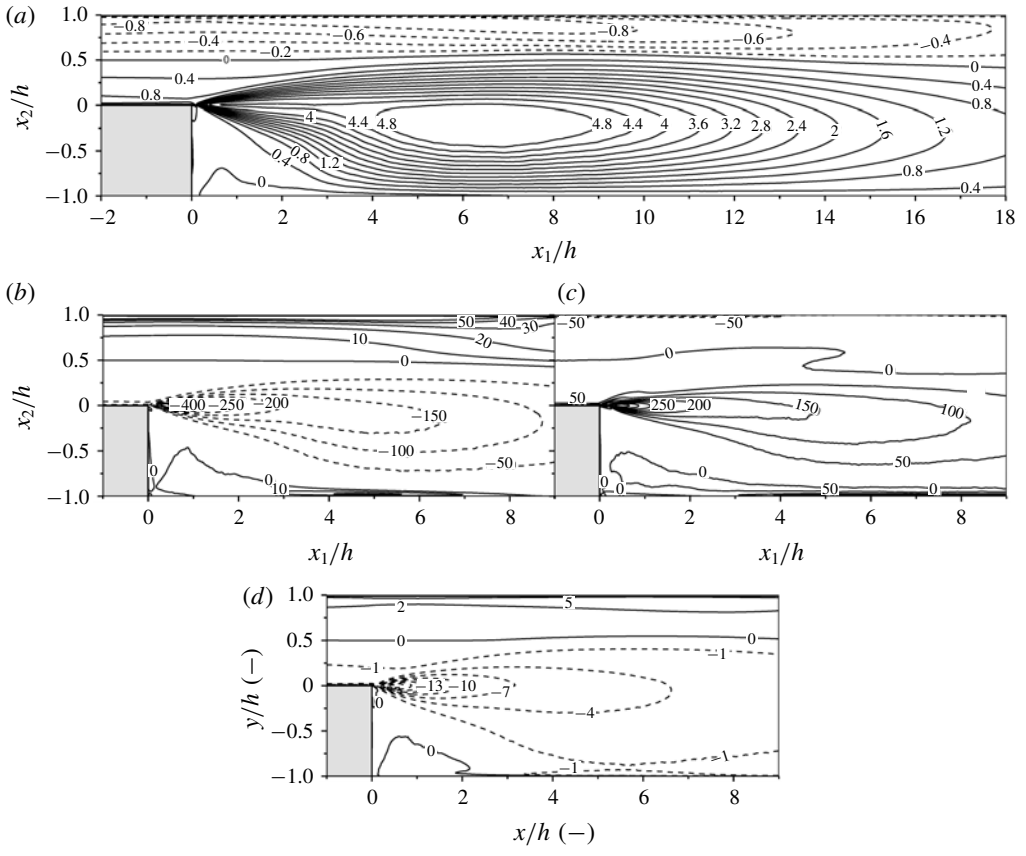

FIGURE 14. Reynolds stresses $-\langle u_1' u_2' \rangle / u_\tau^2$ (*a*) and their associated transport source–sink terms scaled using u_τ^3/h: production $\langle P_{12} \rangle$ (*b*), pressure–strain $\langle \Pi_{12} \rangle$ (*c*) and dissipation $\langle \varepsilon_{12} \rangle$ (*d*). Dashed lines depict negative values.

BFS experimental study. Finally, the offset observed between both $\Delta\delta_2$ approaches does not seem to be critical, as both linear distributions present a similar slope. This indicates that in both cases the elongation ratio, $\Delta\delta_1/\Delta\delta_2$, has a similar growing trend ($\sim$2). However, this correlation is lost downstream of the studied region ($x_1 > 1.6h$), where the free shear layer is no longer present.

5. Conclusions

A DNS of a BFS with a $ER = 2$ has been carried out at $Re_\tau = 395$, defining a case close to the X_r asymptotic behaviour. A turbulent channel flow has been used as an inflow, which has been obtained from a previous simulation. The flow performance $1h$ downstream of the inflow has shown a good agreement with the well-known benchmark results provided by Moser *et al.* (1999), indicating no need for a recovery region. During the verification part other parameters have also been discussed: the time integration period, domain dimensions and mesh resolution. All tests have provided reasonable results, demonstrating that the parameter values satisfy the challenging DNS requirements. Once verified, the DNS results have been compared with the experimental and numerical studies present in the literature.

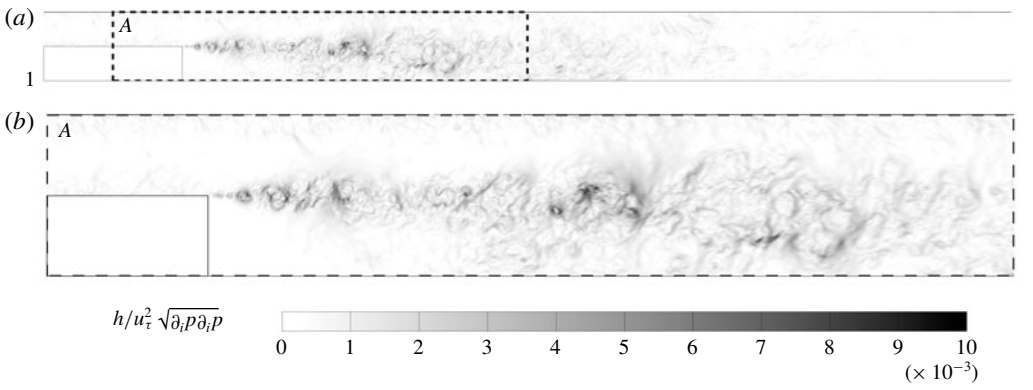

FIGURE 15. Instantaneous magnitude of the dimensionless pressure gradient in a large part of the BFS domain (*a*), and a detailed view (*A*) of the sudden expansion (*b*). The intensity of the fluctuation is denoted by the grey scale bar. See the film attached in the paper data base (Pont-Vílchez *et al.* 2018).

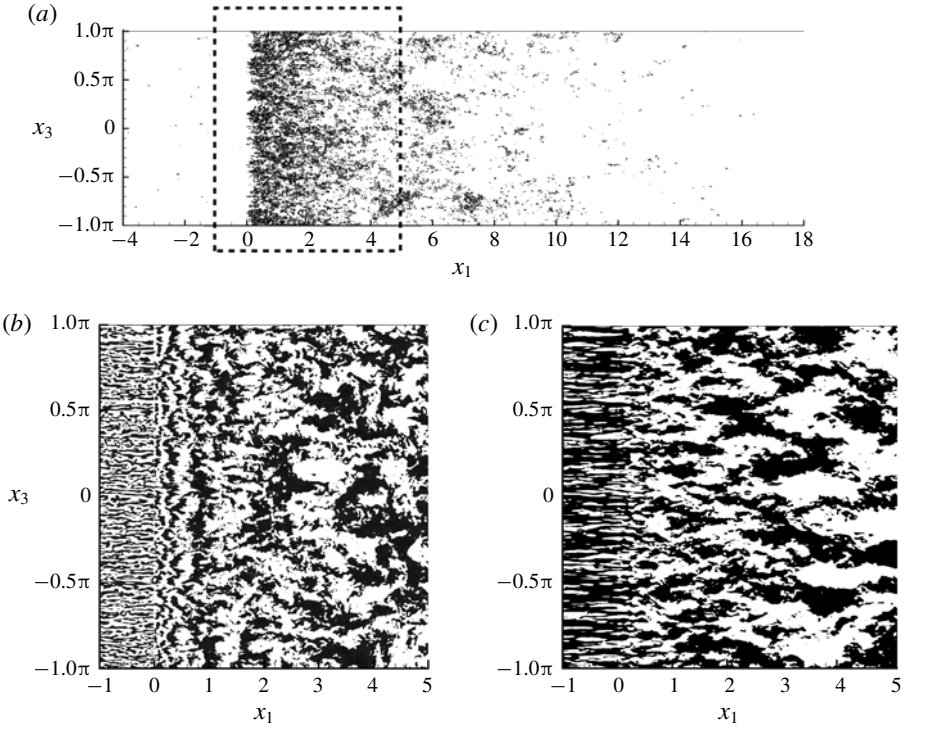

FIGURE 16. A slice parallel to the lower wall at $x_2^+ = 1$ showing instantaneous views of the Q-invariant (*a*), u_2' (*b*) and u_1' (*c*). Black zones denote the highest values of the Q-invariant at the top figure and positive values at the bottom ones.

Besides presenting good agreement with the experimental results, agreement in the X_r asymptotic behaviour zone has also been observed. In addition, numerical benchmark results have also been considered, i.e. Barri *et al.* (2010). The author provided

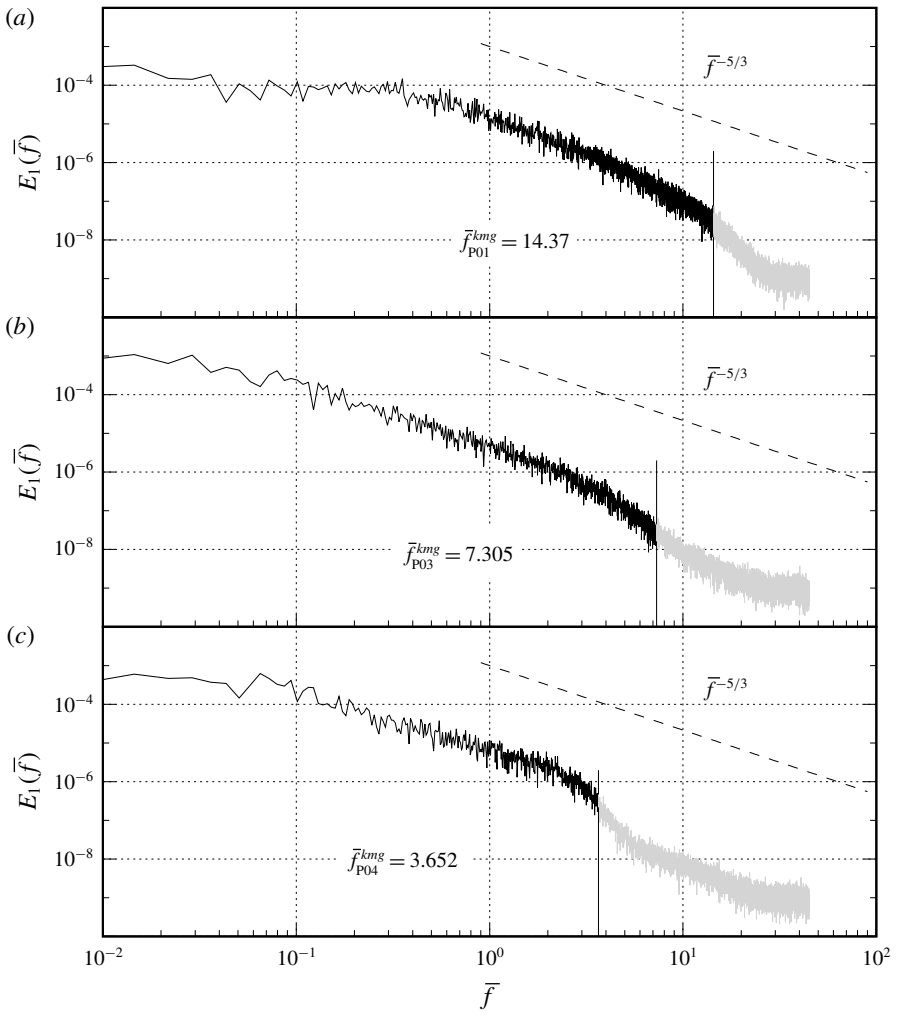

FIGURE 17. Normalized turbulent kinetic energy (E_1) versus normalized temporal frequency ($\bar{f} = fh/U_b$) at P01 (*a*), P03 (*b*) and P04 (*c*). The dashed lines represent the expected turbulence decay behaviour at the inertial region ($\bar{f}^{-5/3}$), whereas $\bar{f}^{kmg}_{\mathrm{P0}N}$ denotes the local Kolmogorov temporal frequency at probe N.

DNS results of a BFS with $ER = 2$, considering a turbulent inflow at $Re_\tau = 180$. In particular, the present DNS exhibited a significant reduction of the $\langle C_f \rangle$ peak in the recirculation region. This phenomenon was previously reported by Jovic & Driver (1994) in experimental work. Regarding the complexity of the flow dynamics, instantaneous views in the spanwise and normal direction have shown the evolution of the flow structures in the streamwise direction. The Kelvin–Helmholtz instabilities can be distinguished in those planes, but they have not been detected in the kinetic energy spectra. However, their rates of growth have been identified through two-point correlations in the streamwise and normal directions. A switching from circular to elliptical structures has been detected close to the step edge (up to $\sim 0.4h$) produced by the advection velocity and the vortex pairing phenomenon. Finally, the elliptical

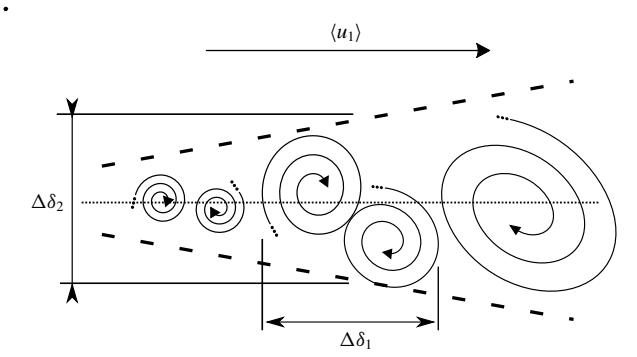

FIGURE 18. Schematic view of the Kelvin–Helmholtz vortices in a shear layer, where $\Delta\delta_1$ and $\Delta\delta_2$ represent a estimation of the vortex size in the streamwise and normal directions, respectively.

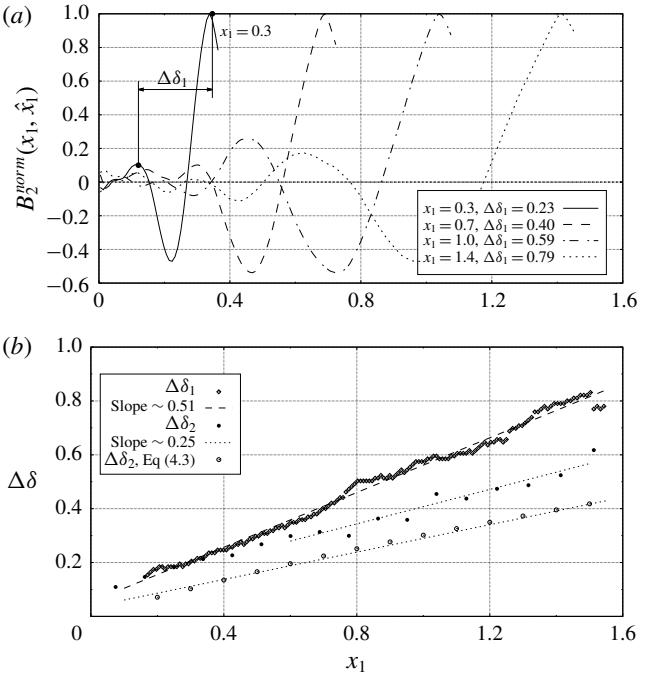

FIGURE 19. An example showing how $\Delta\delta_1$ have been assessed using the two-point correlation at the shear layer (*a*). Estimation of the *KH* rate of growth ($\Delta\delta_1$, $\Delta\delta_2$) along the streamwise direction (*b*), which is schematically depicted in figure 18.

shape trend agrees with the experimental observations carried out by Winant & Browand (1974), showing a major-to-minor axis ratio limit close to 2.

Acknowledgements

This work has been financially supported by the Ministerio de Economía y Competitividad, Spain (no. ENE2017-88697-R). A.P.-V. is supported by a FI-DGR

2016 predoctoral contract financed by Generalitat de Catalunya, Spain. F.X.T. is supported by a Ramón y Cajal postdoctoral contract (no. RYC-2012-11996) financed by the Ministerio de Economía y Competitividad, Spain. The authors thankfully acknowledge the computer resources at MareNostrum and the technical support provided by the Barcelona Supercomputing Centre (RES-FI-2017-2-0041).

REFERENCES

ARMALY, B. F., DURST, F., PEREIRA, J. C. F. & SCHONUNG, B. 1983 Experimental and theoretical investigation of backward-facing step flow. *J. Fluid Mech.* **127**, 473–496.

BARRI, M., EL KHOURY, G. K., ANDERSSON, H. I. & PETTERSEN, B. 2009 Inflow conditions for inhomogeneous turbulent flows. *Intl J. Numer. Meth. Fluids* **60** (2), 227–235.

BARRI, M., EL KHOURY, G. K., ANDERSSON, H. I. & PETTERSEN, B. 2010 DNS of backward-facing step flow with fully turbulent inflow. *Intl J. Numer. Meth. Fluids* **64** (7), 777–792.

BISWAS, G., BREUER, M. & DURST, F. 2004 Backward-facing step flows for various expansion ratios at low and moderate Reynolds numbers. *Trans. ASME J. Fluids Engng* **126** (3), 362–374.

CHORIN, A. J. 1968 Numerical solution of the Navier–Stokes equations. *Math. Comput.* **22**, 745–762.

DE BREDERODE, V. & BRADSHAW, P. 1972 Three-dimensional flow in nominally two-dimensional separation bubbles. I. Flow behind a rearward-facing step. *Tech. Rep.*, IC Aero Rep 72-19, Imperial College, London.

DRIVER, D. M. & SEEGMILLER, H. L. 1985 Features of a reattaching turbulent shear layer in divergent channel flow. *AIAA J.* **23** (2), 163–171.

DURST, F. & TROPEA, C. 1981 Turbulent backward-facing step flows in two-dimensional ducts and channels. In *Proceedings of Turbulent Shear Flows, 3, Symposium*, University of California, Davis, pp. 18.1–18.5.

EATON, J. K. & JOHNSTON, J. P. 1980 Turbulent flow reattachment: an experimental study of the flow and structure behind a backward facing step. *Rep*. MD-39, Dept of Mech Engng, Stanford University, Stanford, CA.

GOROBETS, A., TRIAS, F. X. & OLIVA, A. 2013 A parallel MPI+OpenMP+OpenCL algorithm for hybrid supercomputations of incompressible flows. *Comput. Fluids* **88**, 764–772.

GRITSKEVICH, M. S., GARBARUK, A. V., SCHÜTZE, J. & MENTER, F. R. 2012 Development of DDES and IDDES formulations for the k-ω shear stress transport model. *Flow Turbul. Combust.* **88** (3), 431–449.

JOVIC, S. & DRIVER, D. 1994 Backward-facing step measurements at low Reynolds number, $Reh =$ 5000. *Nasa Tech. Mem.* (February).

JOVIC, S. & DRIVER, D. 1995 Reynolds number effect on the skin friction in separated flows behind a backward-facing step. *Exp. Fluids* **18** (6), 464–467.

KASAGI, N. & MATSUNAGA, A. 1995 Three-dimensional particle-tracking velocimetry measurement of turbulence statistics and energy budget in a backward-facing step flow. *Intl J. Heat Fluid Flow* **16** (6), 477–485.

KIM, J. & MOIN, P. 1985 Application of a fractional-step method to incompressible Navier–Stokes equations. *J. Comput. Phys.* **123**, 308–323.

KOSTAS, J., SORIA, J. & CHONG, M. 2002 Particle image velocimetry measurements of a backward-facing step flow. *Exp. Fluids* **33** (6), 838–853.

KUEHN, D. M. 1980 Effects of adverse pressure gradient on the incompressible reattaching flow over a rearward-facing step. *AIAA J.* **18** (3), 343–344.

LASHER, W. C. & TAULBEE, D. B. 1992 On the computation of turbulent backstep flow. *Intl J. Heat Fluid Flow* **13** (1), 30–40.

LE, H., MOIN, P. & KIM, J. 1997 Direct numerical simulation of turbulent flow over a backward-facing step. *J. Fluid Mech.* **330**, 349–374.

MERI, A. & WENGLE, H. 2002 DNS and LES of turbulent backward-facing step flow using 2nd-and 4th-order discretization. In *Advances in LES of Complex Flows* (ed. R. Friedrich & W. Rodi), Fluid Mechanics and its Applications, vol. 65, pp. 99–114. Kluwer.

MOCKETT, C., HAASE, W. & SCHWAMBORN, D. 2018 *Go4Hybrid: Grey Area Mitigation for Hybrid RANS-LES Methods*, Notes on Numerical Fluid Mechanics and Multidisciplinary Design, vol. 134. Springer.

MOSER, R. D., KIM, J. & MANSOUR, N. N. 1999 Direct numerical simulation of turbulent channel flow up to $Re_\tau = 590$. *Phys. Fluids* **11**, 943–945.

NADGE, P. M. & GOVARDHAN, R. N. 2014 High Reynolds number flow over a backward-facing step: structure of the mean separation bubble. *Exp. Fluids* **55** (1), 1657–1678.

ÖTÜGEN, M. V. 1991 Expansion ratio effects on the separated shear layer and reattachment downstream of a backward-facing step. *Exp. Fluids* **10** (5), 273–280.

PONT-VÍLCHEZ, A., TRIAS, F. X., GOROBETS, A. & OLIVA, A. 2018 Direct numerical simulation results presented in this paper. http://www.cttc.upc.edu/downloads/BFS_Ret395_ER2.

SCHÄFER, F., BREUER, M. & DURST, F. 2009 The dynamics of the transitional flow over a backward-facing step. *J. Fluid Mech.* **623**, 85–119.

SHUR, M. L., SPALART, P. R., STRELETS, M. K. & TRAVIN, A. K. 2008 A hybrid RANS-LES approach with delayed-DES and wall-modelled LES capabilities. *Intl J. Heat Fluid Flow* **29** (6), 1638–1649.

SHUR, M. L., SPALART, P. R., STRELETS, M. K. & TRAVIN, A. K. 2015 An enhanced version of des with rapid transition from RANS to les in separated flows. *Flow Turbul. Combust.* **95** (4), 709–737.

SPALART, P. R., DECK, S., SHUR, M. L., SQUIRES, K. D., STRELETS, M. K. & TRAVIN, A. 2006 A new version of detached-eddy simulation, resistant to ambiguous grid densities. *Theor. Comput. Fluid Dyn.* **20** (3), 181–195.

SPALART, P. R., JOU, W. H., STRELETS, M. & ALLMARAS, S. R. 1997 Comments on the feasibility of LES for wings, and on a hybrid RANS/LES approach. In *Advances in DES/LES* (ed. C. Liu & Z. Liu). Greyden Press.

SPEZIALE, C. G. & NGO, T. 1988 Numerical solution of turbulent flow past a backward facing step using a nonlinear K-ϵ model. *Intl J Engng Sci.* **26** (10), 1099–1112.

THANGAM, S. & SPEZIALE, C. G. 1992 Turbulent flow past a backward-facing step – a critical evaluation of two-equation models. *AIAA J.* **30** (5), 1314–1320.

TRIAS, F. X., GOROBETS, A. & OLIVA, A. 2015 Turbulent flow around a square cylinder at Reynolds number 22 000: a DNS study. *Comput. Fluids* **123** (22), 87–98.

TRIAS, F. X. & LEHMKUHL, O. 2011 A self-adaptive strategy for the time-integration of Navier–Stokes equations. *Numer. Heat Transfer* B **60** (2), 116–134.

TRIAS, F. X., SORIA, M., OLIVA, A. & PÉREZ-SEGARRA, C. D. 2007 Direct numerical simulations of two- and three-dimensional turbulent natural convection flows in a differentially heated cavity of aspect ratio 4. *J. Fluid Mech.* **586**, 259–293.

VERSTAPPEN, R. W. C. P. & VELDMAN, A. E. P. 2003 Symmetry-preserving discretization of turbulent flow. *J. Comput. Phys.* **187**, 343–368.

VREMAN, A. W. & KUERTEN, J. G. M. 2014 Comparison of direct numerical simulation databases of turbulent channel flow at $Re_\tau = 180$. *Phys. Fluids* **26** (1), 1–22.

WINANT, C. D. & BROWAND, F. K. 1974 Vortex pairing: the mechanism of turbulent mixing-layer growth at moderate Reynolds number. *J. Fluid Mech.* **63** (2), 237–255.